MATERIALS SCIENCE

Catalysis-tunable Heusler alloys in selective hydrogenation of alkynes: A new potential for old materials

Takayuki Kojima[1,2]*, Satoshi Kameoka[2], Shinpei Fujii[3], Shigenori Ueda[4,5], An-Pang Tsai[2]

Heusler alloys (X_2YZ) are well-established intermetallic compound materials in various fields because their function can be precisely adjusted by elemental substitution (e.g., $X_2YZ_{1-x}Z'_x$). Although intermetallic compound catalysts started attracting attention recently, catalysis researchers are not familiar with Heusler alloys. We report their potential as novel catalysts focusing on the selective hydrogenation of alkynes. We found that Co_2MnGe and Co_2FeGe alloys have great alkene selectivity. Mutual substitution of Mn and Fe ($Co_2Mn_xFe_{1-x}Ge$) enhanced the reaction rate without changing selectivity. The substitution of Ga for Ge decreased the selectivity but increased the reaction rate monotonically with Ga composition. Elucidation of these mechanisms revealed that the fine tuning of catalytic properties is possible in Heusler alloys by separately using ligand and ensemble effects of elemental substitution.

INTRODUCTION

Heusler alloys (X_2YZ) are intermetallic compounds that were discovered by Heusler in 1903 (*1*). The crystal structure of the $L2_1$ Heusler alloy is illustrated in Fig. 1 (*2*). The Cu_2MnAl Heusler alloy and other Heusler alloys have attracted attention because they exhibit ferromagnetism even without ferromagnetic elements. They are now particularly attractive in various research fields, including spintronics (*3*), thermoelectrics (*4*), and ferromagnetic shape memory alloys (*5*). Their features include having many possible sets of elements, as shown in Fig. 1 [the details are reported by Yin *et al.* (*6*)], and allowing partial substitution of components (e.g., $X_2YZ_{1-x}Z'_x$), which is used to optimize electronic structures. The first-mentioned feature portends the discovery of novel catalysts, and the second one would enable the fine tuning of catalytic properties because catalysis is governed by the electronic structure (the ligand effect) and by the atomic arrangement at the surface (the ensemble effect).

Intermetallic compounds are attracting much attention as novel catalysts because they form new electronic structures that differ from those of their components and because they have specific surface atomic arrangements (*7*, *8*). To the best of our knowledge, there was no paper regarding Heusler alloys dealing with catalysis until our study. Previously, to represent their potential for new catalysts, we tested the potential of various Heusler alloys for hydrogenation of propyne and oxidation of carbon monoxide (*9*). Since then, we have found that Co_2MnGe and Co_2FeGe are very useful for selective hydrogenation of alkynes and now report that here.

Selective hydrogenation is an important process for removing alkyne impurities from alkene feedstock because the impurities poison the catalyst during alkene polymerization (*10*, *11*). Palladium-based catalysts have been used in industry for selective hydrogenation of ethyne (acetylene) in ethene (ethylene) and propyne (methylacetylene) in propene (propylene) (*10*–*12*). Replacement of Pd with a nonprecious metal is desirable in terms of cost performance and resource availability, and these catalysts have been developed in the laboratory using intermetallic compounds such as NiZn, $NiZn_3$ (*13*), $Al_{13}Fe_4$ (*14*), Ni_3Ga, and Ni_3Sn_2 (*15*). In such binary intermetallics, however, elemental substitution is restricted while keeping the original crystal structure. In contrast, this substitution with a wide composition range of various elements can be done in Heusler alloy catalysts. This would be a unique advantage enabling precise adjustment of the catalytic properties to the target reaction. Here, we demonstrate control of the catalytic properties of Heusler alloys by elemental substitution ($Co_2Mn_xFe_{1-x}Ga_yGe_{1-y}$) in the selective hydrogenation of alkynes (propyne and ethyne).

[1]Frontier Research Institute for Interdisciplinary Sciences, Tohoku University, Sendai 980-8578, Japan. [2]Institute of Multidisciplinary Research for Advanced Materials, Tohoku University, Sendai 980-8577, Japan. [3]Graduate School of Science and Engineering, Kagoshima University, Kagoshima 890-0065, Japan. [4]Research Center for Advanced Measurement and Characterization, National Institute for Materials Science, Tsukuba, Ibaraki 305-0047, Japan. [5]Synchrotron X-ray Station at SPring-8, National Institute for Materials Science, Hyogo 679-5148, Japan.
*Corresponding author. Email: takayuki.kojima.b4@tohoku.ac.jp, takayuki.kojima1130@gmail.com

RESULTS

Hydrogenation of alkyne in the presence of alkene

Figure 2 shows the alkyne conversions and alkene selectivities in the hydrogenations of propyne (C_3H_4) in the presence of propene (C_3H_6), and ethyne (C_2H_2) in the presence of ethene (C_2H_4) for powder samples sieved to a particle size of 20 to 63 μm. Ordinary catalysts such as pure metals usually exhibit high alkene selectivity when alkyne conversion is low, and selectivity decreases as conversion increases (*13*, *16*, *17*) as it does for Co_2FeGa, as shown in Fig. 2F. This behavior is attributed to strongly adsorbed alkyne molecules inhibiting the adsorption of alkene molecules, while a decrease in inhibiters (alkyne) at a high conversion enables alkene adsorption.

In contrast, $Co_2Mn_xFe_{1-x}Ge$ showed high alkene selectivities even at a 100% alkyne conversion (Fig. 2, A to C). This is surprising because the hydrogen/alkyne ratios in the feeds were 400 (0.1% alkyne/10% alkene/40% H_2/He balance), which is much higher than the reported ratios (10 to 20) (*10*, *13*–*15*). In addition, $Co_2Mn_xFe_{1-x}Ge$ poorly catalyzed the hydrogenation of C_3H_6 in the absence of C_3H_4 (0.1% C_3H_6/40% H_2/He balance), which indicates that it has almost no ability to hydrogenate alkenes (fig. S3). Since alkene selectivity usually decreases with the hydrogen/alkyne ratio (*10*, *18*), operating conditions in industrial plants must be precisely controlled to avoid hydrogenating the alkene feedstock and to maximize the removal rate of alkyne (*10*, *11*). Therefore, $Co_2Mn_xFe_{1-x}Ge$ is expected to be useful under any operating conditions.

The Mn substitution for Fe resulted in certain changes in the conversions and selectivities (Fig. 2, A to C). The Ga substitution for Ge increased the conversions at lower temperatures and decreased the selectivities at higher temperatures (Fig. 2, D to F).

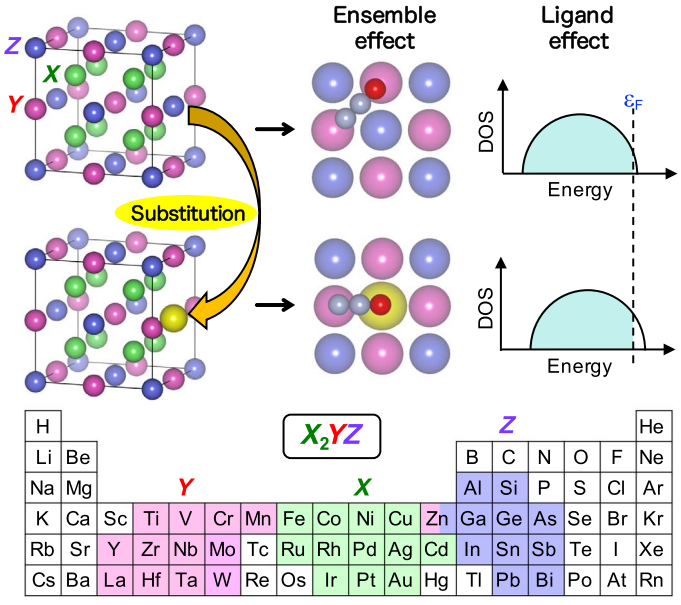

Fig. 1. Concept of this study. Effects of elemental substitution are schematically illustrated with the Heusler alloy's crystal structure ($L2_1$-type X_2YZ) (*2*). Periodic table represents typical elements consisting of *X*, *Y*, and *Z* (color painted). Other elements such as lanthanoids and those in groups 1 and 2 are also possible components of Heusler alloys [see (*6*)].

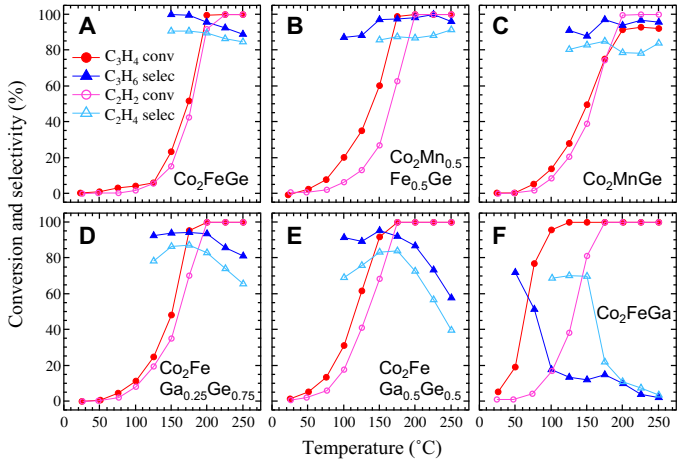

Fig. 2. Results of alkyne hydrogenation in the presence of alkene. Alkyne conversions (circles) and alkene selectivities (triangles) for (**A**) Co_2FeGe, (**B**) $Co_2Mn_{0.5}Fe_{0.5}Ge$, (**C**) Co_2MnGe, (**D**) $Co_2FeGa_{0.25}Ge_{0.75}$, (**E**) $Co_2FeGa_{0.5}Ge_{0.5}$, and (**F**) Co_2FeGa. Closed and open symbols represent results for hydrogenations of C_3H_4 in C_3H_6 and C_2H_2 in C_2H_4, respectively. Reactants were [0.1% alkynes/10% alkenes/40% H_2/He balance]. Selectivities in low-conversion region are not shown due to large errors.

Hydrogenation of C_3H_4 in the absence of C_3H_6

To determine the effects of elemental substitution, C_3H_4 hydrogenation in the absence of C_3H_6 was investigated, excluding the complexities due to the presence of alkene molecules and the oligomerization that often occurs in C_2H_2 hydrogenation (*10*, *11*, *18*). Figure 3 shows the effects of Mn substitution for Fe ($Co_2Mn_xFe_{1-x}Ge$; Fig. 3A) and Ga substitution for Ge ($Co_2FeGa_yGe_{1-y}$; Fig. 3B) on the reaction rates of C_3H_4 normalized to the values for Co_2FeGe and on C_3H_6 selectivities with a C_3H_4 conversion of 100% at 200°C (overall data are shown in fig. S1). Similar to the results shown in Fig. 2, $Co_2Mn_xFe_{1-x}Ge$ showed high C_3H_6 selectivity, and Ga substitution increased the rate but decreased the selectivity. The Mn substitution did not change the selectivity but increased the rate in the partial substitution range ($0.25 \leq x \leq 0.75$). These tendencies were also observed for $Co_2Mn_xFe_{1-x}Ga$ and $Co_2MnGa_yGe_{1-y}$ (fig. S2), indicating that the Mn-Fe substitution and the Ga-Ge substitution act independently of each other.

Relationship between electronic structure and activation energy

Considering the features of Heusler alloys, the substitution effects most likely originated from the electronic structure. The *d*-band theory combined with the Brønsted-Evans-Polanyi (BEP) relation is widely accepted to explain the relationship between catalytic activity and electronic structure (*19*–*21*). This theory suggests a linear relationship between the activation energy (E_a) and the mean energy of the *d*-band (ε_d, so-called *d*-band center). Figure 4 (A1 and A2) shows the densities of states (DOSs) calculated using density functional theory; they reveal continuous band shifts with Mn and Ga compositions. This behavior was verified by hard x-ray photoelectron spectroscopy (HAXPES) of the valence bands, as shown in Fig. 4 (B1 and B2), which indicated that the electronic structures were properly controlled by elemental substitutions in actual samples. The high intensities in the high binding energy region were due to large photoionization cross sections of the *s*-bands under this measurement condition (*22*). Figure 4C shows the E_a obtained experimentally for the C_3H_4 hydrogenation and the ε_d estimated from the partial DOSs of the *d*-bands. Their changes with substitution were similar. The E_a versus ε_d plot in Fig. 4D shows a linear relationship, indicating that changes in the electronic structure contributed to changes in the catalytic properties.

DISCUSSION

Validity of relationship between E_a and ε_d

To confirm the validity of the changes in E_a due to ε_d, we look for insights into the reaction mechanism. The reaction orders with respect to C_3H_4 and H_2 were roughly estimated to be −0.2 to 0 and 0.8 to 1, respectively (fig. S5 and table S1). These values are usually obtained for pure transition metal catalysts (*17*, *23*). The adsorption processes of C_3H_4 and H_2 were considered to be almost noncompetitive because the C_3H_4 reaction order is typically −1 or −2 for competitive adsorption in the Langmuir-Hinshelwood (LH) model. In our case, H_2 (g) ⇒ 2H (ad) or C_3H_4 (ad) + 2H (ad) ⇒ C_3H_6 (ad) is likely to be the rate-determining step corresponding to the reaction orders obtained, and following equations were derived under the assumption of the LH model with noncompetitive adsorption (see the Supplementary Materials) (*23*).

[H_2 (g) ⇒ 2H (ad) is rate determining]

$$r = kP_{H2} = P_{H2}\ A\exp\left(-\frac{E_{a,H2,ad}}{RT}\right) \quad (1)$$

[C_3H_4 (ad) + 2H (ad) => C_3H_6 (ad) is rate determining]

$$r = kK_{H2,ad}P_{H2} = P_{H2}\ A\exp\left(\frac{\Delta S^{\circ}_{H2,ad}}{R}\right)\exp\left(-\frac{E_{a,s} + \Delta H^{\circ}_{H2,ad}}{RT}\right) \quad (2)$$

where r, k, P_{H2}, and $K_{H2,ad}$ are the reaction rate, the rate constant, the partial pressure of H_2, and the equilibrium constant for dissociative adsorption of H_2, respectively. The k is expanded to the Arrhenius equation using the activation energy of the rate-determining step ($E_{a,H2,ad}$ or $E_{a,s}$) and a frequency factor (A). The $K_{H2,ad}$ is expanded to two exponential parts containing the standard entropy ($\Delta S°_{H2,ad}$) and enthalpy ($\Delta H°_{H2,ad}$) of the H_2 adsorption. Accordingly, the E_a value obtained experimentally is described by $E_a = E_{a,s} + \Delta H°_{H2,ad}$, when r follows Eq. 2.

The d-band theory and the BEP relation indicate that increase in ε_d decreases (negatively increases) the H_2 adsorption energy and eventually decreases $E_{a,H2,ad}$. Thus, Eq. 1 agrees with the trend in Fig. 4D. In the case of Eq. 2, increase in ε_d strengthens adsorption of C and H atoms, which probably increases $E_{a,s}$ as reported on the hydrogenation of C_2H_x molecules (*24*). Thus, the increase in ε_d should decrease $\Delta H°_{H2,ad}$ more than the increase in $E_{a,s}$ to produce the trend in Fig. 4D. According to the literature (*20*, *25*, *26*), $E_{a,s} = 114 + 13\varepsilon_d$ [kJ mol^{-1}] and $\Delta H°_{H2,ad} = -106 - 31\varepsilon_d$ [kJ mol^{-1}] (unit of ε_d, eV) can be obtained, although the $E_{a,s}$ versus ε_d relationship is rough because they were extrapolated from only four data points in two reports (*20*, *25*). The slope of $E_{a,s} + \Delta H°_{H2,ad} = 8 - 18\varepsilon_d$ agrees well with the slope of the experimental values in Fig. 4D. Therefore, both Eqs. 1 and 2 qualitatively explain the experimental results. However, it is hard to conclude which model is more reasonable, because there is uncertainty regarding the reaction mechanism (e.g., eq. S3) and the adsorption configurations of C_3H_4 and H_2 for Heusler alloys differ from those reported for pure metals (discussed below).

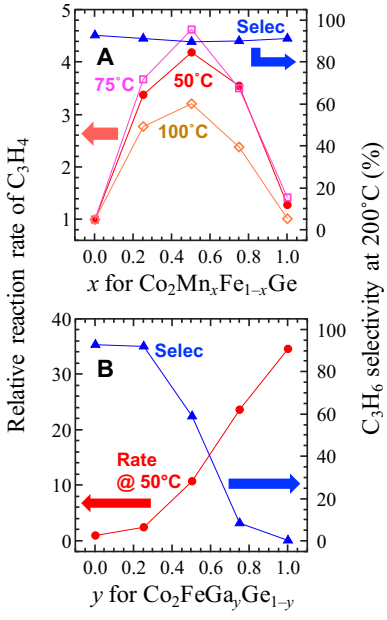

Fig. 3. Effects of elemental substitution in C_3H_4 hydrogenation in the absence of C_3H_6. Changes in reaction rates of C_3H_4 per surface area and selectivities for C_3H_6 due to (**A**) Mn substitution ($Co_2Mn_xFe_{1-x}Ge$) and (**B**) Ga substitution ($Co_2FeGa_yGe_{1-y}$). The reaction rates were normalized by those of Co_2FeGe ($x = y = 0$). In (A), the rates at 100°C (diamonds), 75°C (squares), and 50°C (circles) are shown. Blue triangles represent the selectivities for 100% C_3H_4 conversion at 200°C. The reactant was [0.1% C_3H_4/40% H_2/He balance].

Effects of Mn substitution

Although uncertainty remains, the reaction rate would basically follow Eq. 1 or Eq. 2. That is, the rate should monotonically increase with Mn composition (x) since the E_a value decreased with x, but the rate turned downward at $x > 0.5$, as shown in Fig. 3A. This behavior is attributed to the enthalpy-entropy compensation effect often observed in various thermodynamic phenomena including catalytic reactions (*27*–*29*). Although the mechanism of this effect is still not fully understood, taking the H_2 adsorption as an example, we can qualitatively understand that strengthening the binding between the catalyst and H atoms decreases (negatively increases) $\Delta H°_{H2,ad}$ and also decreases $\Delta S°_{H2,ad}$ since a stronger binding reduces the degree of freedom of adsorbed H atoms. Therefore, a decrease in $\Delta S°_{H2,ad}$ due to the compensation effect might suppress an increase in the rate if the rate followed Eq. 2. According to the transition state theory (*27*), $A \propto \exp(\Delta S_{TS}/R)$ and $\exp(-E_a/RT) \propto \exp(-\Delta H_{TS}/RT)$ are derived, where ΔS_{TS} and

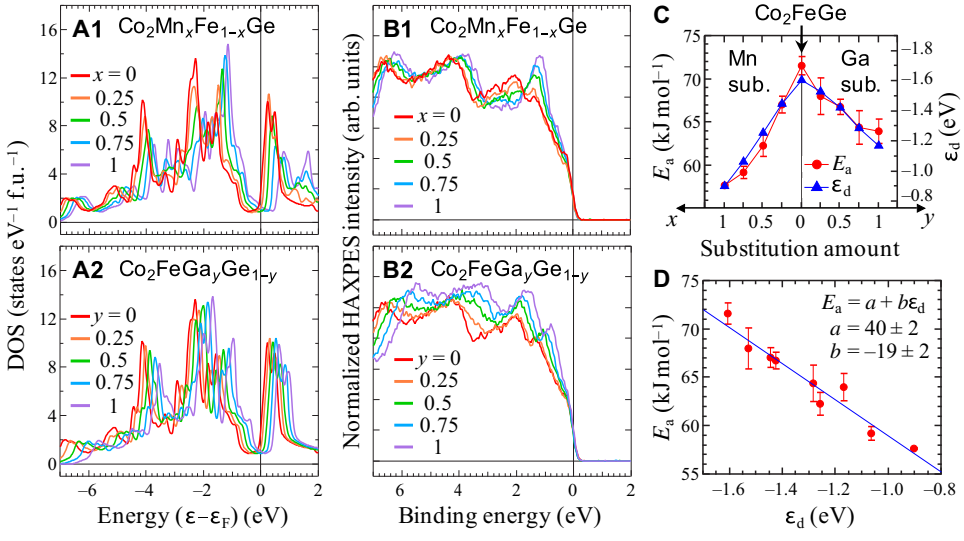

Fig. 4. Electronic structures and activation energy for C_3H_4 hydrogenation in the absence of C_3H_6. (**A1** and **A2**) DOSs. f.u., formula unit. (**B1** and **B2**) Valence band HAXPES spectra. (**C**) Changes in experimental E_a and calculated ε_d due to Mn and Ga substitutions. (**D**) Relationship between E_a and ε_d.

ΔH_{TS} are changes in entropy and enthalpy in the transition state, respectively. Thus, the compensation could happen even if the rate follows Eq. 1.

In many cases of this compensation, the changes in enthalpy and entropy show a linear relationship, $dH = TdS$, corresponding to full compensation (*28*). In Fig. 3A, the compensation for $x = 1$ was apparently almost full, while that for $0.25 \leq x \leq 0.75$ was not full. This behavior is not strange given that a nonlinear relationship between dH and dS is sometimes observed (*29*). However, the reason for this behavior was not elucidated in this study due to various complexities, including the uncertainty of the reaction model and the compensation between $E_{a,s}$ and ΔS_{TS} in the case of Eq. 2. We suppose that the behavior is due to a random distribution of Mn and Fe atoms at *Y* sites (of X_2YZ), which would cause the interactions between adsorbed species to be inhomogeneous, because the interaction between adsorbates affects kinetics and thermodynamics on the surface such that the enthalpy and entropy of adsorption depend on the adsorbate coverage (*30*, *31*).

Effects of Ga substitution

In contrast to Mn substitution, Ga substitution increased the reaction rate monotonically with Ga composition (*y*) along with the decrease in E_a (Figs. 3B and 4C), which seems reasonable. However, why was there no compensation for the rate increase? Furthermore, why did the selectivity decrease significantly? We attribute these results to the same mechanism discussed below. In the hydrogenation of C_3H_6 in the absence of C_3H_4, the C_3H_6 conversion was very low for the Co_2FeGe, while it monotonically increased with Ga substitution (fig. S3). This indicates that Ga substitution brought the ability to adsorb C_3H_6.

In selective hydrogenation of C_2H_2 using Pd-based catalysts, the high C_2H_4 selectivity is attributed to a small adsorption site surrounded by poisonous species that sterically hinder the adsorption of larger molecules, C_2H_4, but allow the adsorption of smaller molecules, C_2H_2 (*10*, *11*). Figure 5A shows schematic illustrations of close-packed (110) surfaces for Co_2FeGe, $Co_2FeGa_{0.5}Ge_{0.5}$, and Co_2FeGa. Assuming that Ge atoms do not have the ability to adsorb hydrocarbons while Ga atoms do, the size of sites available for adsorption is small on Co_2FeGe(110), while it is enlarged by Ga substitution as we can see on $Co_2FeGa_{0.5}Ge_{0.5}$(110). We believe that this is the mechanism of the high alkene selectivity for $Co_2Mn_xFe_{1-x}Ge$ and the reduction in selectivity due to Ga substitution. Under this assumption, the increase in the rate due to Ga substitution can also be explained by an increase in the number of sites available for adsorption.

This hypothesis is supported by theoretical calculation. A series of theoretical studies by Krajčí and Hafner revealed that typical element atoms such as Al, Ga, and Zn contribute to the adsorption of hydrocarbons on the surface of intermetallic compounds with transition metals (*32*–*34*). Taking the surface of $Al_{13}Co_4$ as an example, we see that C_2H_2 molecules adsorb on a bridge site between two Al atoms rather than on a site containing Co atoms (*32*, *33*). In terms of the electronic structure, the hydrocarbon adsorption ability of typical elements can be related to the hybridization of the *p*-bands of the typical elements with the *d*-bands of the transition metals (*32*). Figure 5B shows the *p*-bands of Ge in Co_2FeGe and of Ga in Co_2FeGa for (110) surfaces. We can see that the Ga *p*-band is located at a shallower level from the Fermi level than the Ge *p*-band. The Ga atoms have a higher hydrocarbon adsorption ability than Ge atoms, similar to the *d*-band theory. Therefore, the assumption of differing adsorption abilities between Ga and Ge is reasonable.

Fig. 5. Effects of Ga substitution for Ge of Co_2FeGe. (**A**) Schematic illustration of (110) surfaces for Co_2FeGe, $Co_2FeGa_{0.5}Ge_{0.5}$, and Co_2FeGa. (**B**) Local partial DOSs (LPDOSs) of Ge at Co_2FeGe(110) (blue) and Ga at Co_2FeGa(110) (red) surfaces.

CONCLUSIONS

Here, we have presented the advantage of using Heusler alloys as new catalysts and have demonstrated the control of catalytic properties by elemental substitution in the selective hydrogenation of alkyne. The $Co_2Mn_xFe_{1-x}Ge$ catalysts showed high alkene selectivity even with 100% alkyne conversion and even with a very high H_2/alkyne ratio of 400; they poorly catalyzed the C_3H_6 hydrogenation in the absence of C_3H_4. These results indicate that the $Co_2Mn_xFe_{1-x}Ge$ catalysts can be useful under any operating condition.

The elemental substitution resulted in a change in E_a along with ε_d, which indicates that the electronic structure was accurately controlled and that it contributed to the catalytic properties. The significant increase in reaction rate and decrease in selectivity with Ga substitution for Ge were attributed to the difference in hydrocarbon adsorption ability between Ga and Ge atoms in $Co_2FeGa_yGe_{1-y}$. This seems to be an ensemble effect in a conventional manner, in contrast to the effect of Mn-Fe substitution changing only the electronic structure, the so-called ligand effect. This means that Heusler alloys can separately use the ensemble and ligand effects depending on the purpose. Although Mn substitution for Fe did not greatly increase the reaction rate with the decrease in E_a probably due to the compensation effect, this ligand effect could be effective for other reactions in which a correspondence between an activity and an electronic structure-derived parameter (e.g., E_a, ε_d, and adsorption energy) has been experimentally

observed, such as methanation from CO and an oxygen reduction reaction (*21*, *35*).

In addition, Heusler alloys can be used as a well-defined platform for revealing the catalysis of intermetallic compounds because catalysis with various electronic structures and various surface elements can be investigated using elemental substitution under the same crystal structure. Last, since many Heusler alloys are free of precious metals, as shown in Fig. 1, the future development of new practical catalysts is promising.

MATERIALS AND METHODS

Sample preparation and characterization

Heusler alloy ingots were prepared from pure metallic sources (purity, >99.9%) by arc melting followed by annealing during which the condition was typically 1000°C for 72 hours followed by 600°C for 72 hours and then 500°C for 72 hours under an Ar atmosphere. Powder catalysts were obtained by crushing the ingots using a mortar and pestle, followed by sieving to a particle size of 20 to 63 μm.

The structural properties were evaluated by x-ray diffraction (XRD) using powders with a size of <20 μm after removing the strain and defects by annealing at 600°C for 1 hour under an H_2 atmosphere. The XRD was performed using the Bragg-Brentano geometry with Cu Kα radiation (Rigaku, Ultima IV diffractometer). The XRD patterns shown in fig. S6 indicate the formation of a (nearly) single phase $L2_1$ structure for all samples, although negligible unknown peaks were detected in several samples. The degree of atomic ordering was evaluated using Webster's model with factors S and α. The S factor corresponds to a long-range order parameter in a binary alloy. $S = 1$ ensures that all Co atoms occupy the X sites in X_2YZ, that is, the ordering between the Co and YZ elements. $S = 0$ means that all atoms randomly occupy the X, Y, and Z sites. α describes the "disordering" between the Y and Z elements. $\alpha = 0.5$ means no Y-Z order, while $\alpha = 0$ means no Y-Z "disorder." Thus, satisfaction of both $S = 1$ and $\alpha = 0$ means perfect $L2_1$ ordering. These factors were estimated by using

$$S = \sqrt{\frac{(I_{200}/I_{400})_{exp}}{(I_{200}/I_{400})_{cal}}} \quad (3)$$

$$(1 - 2\alpha)S = \sqrt{\frac{(I_{111}/I_{fund})_{exp}}{(I_{111}/I_{fund})_{cal}}} \quad (4)$$

where I_{200}, I_{111}, and I_{400} are the integrated intensities of the 200 and 111 superlattice peaks and the 400 fundamental peak, respectively, and I_{fund} is the fundamental peak of 220, 400, 422, or 440 diffraction. The numerators are experimental values, while the denominators are theoretical values in the perfect-order cases calculated from atomic scattering factors including anomalous scattering terms, the multiplicity factor, the Lorentz-polarization factor, and the Debye-Waller factors. The obtained S and α factors are listed in table S1. Sufficiently high S and low α were obtained, indicating high ordering into the $L2_1$ structure. Kojima *et al.* (*9*) for more information about the estimation of S and α.

The surface area of the catalyst after the C_3H_4 hydrogenation in the absence of C_3H_6 (table S1) was estimated using the Brunauer-Emmett-Teller method with Kr adsorption (MicrotracBEL, BELSORP-max volumetric adsorption instrument) to calculate the reaction rates shown in Fig. 3 and fig. S2.

Catalytic measurements and evaluation

The catalytic properties were evaluated for the reactions using [0.1% C_3H_4/40% H_2/He balance], [0.1% C_3H_6/40% H_2/He balance], [0.1% C_3H_4/10% C_3H_6/40% H_2/He balance], and [0.1% C_2H_2/10% C_2H_4/40% H_2/He balance] reactants. The measurements were conducted in standard flow reactors with gas chromatographs: (i) an Agilent 490 Micro GC equipped with a thermal conductivity detector (TCD) and a PoraPLOT Q column for the C_3H_4 hydrogenation and (ii) a Shimadzu GC-8A equipped with a TCD and a Shincarbon-ST column for the C_2H_2 hydrogenation. The catalyst (400 mg) was supported on quartz wool in a quartz tube with an internal diameter of 4 mm and surrounded by an electric furnace. After the catalyst was heated under an H_2 gas flow at 600°C for 1 hour to remove the surface oxides, the reactant mixture was introduced at 30 ml min^{-1} (standard temperature and pressure) at ambient temperature and pressure through mass flow controllers into the catalyst channel (space velocity, about 20,000 $hours^{-1}$). The catalyst was then left standing for 1 hour, and then, analysis of the gaseous species and heating were started. The unreacted reactants and products were analyzed 30 min after heating ended at every 25°C interval from 25° to 250°C.

The alkyne conversion and the alkene selectivity were estimated by using

$$\text{Conversion} = 100 \times \frac{C_{feed} - C_{unreact}}{C_{feed}}[\%] \quad (5)$$

$$\text{Selectivity} = 100 \times \frac{C_{alkene}}{C_{alkene} + C_{alkane} + C_{lost}}[\%]$$

(without alkene feed) (6)

$$\text{Selectivity} = 100 \times \frac{C_{feed} - C_{unreact}}{C_{feed} - C_{unreact} + C_{alkane}}[\%]$$

(with alkene feed) (7)

where C_{feed}, $C_{unreact}$, C_{alkene}, and C_{alkane} were the concentrations of the feed alkyne, the unreacted alkyne, the produced alkene, and the produced alkane, respectively. C_{lost} in Eq. 6 is the concentration of the carbon species lost due probably to oligomerization ($C_{lost} = C_{feed} - C_{unreact} - C_{alkene} - C_{alkane}$). For the alkyne hydrogenation in the presence of alkene, the alkene selectivity was estimated using Eq. 7 under the assumption that all the reacted alkynes were converted into alkenes and that $C_{lost} = 0$ because the very large amount of the feed alkene made it impossible to estimate small amounts of produced alkene and the lost carbon.

The apparent E_a for the C_3H_4 hydrogenation in the absence of C_3H_6 was evaluated by continuous cyclic measurement with analysis performed at every 1°C during the heating and cooling cycle at a rate of 0.5°C min^{-1} between 50° and 100°C. Appropriate amounts of the catalysts and the flow rates were used so that the conversion was appropriate for estimating the E_a value. The E_a value was estimated by averaging the values for both the heating and cooling processes after the change in the slope of the Arrhenius plot had sufficiently settled, as shown in fig. S4. The values and the ranges of the temperature and the conversion used for the estimation are shown in table S1. The error bar corresponds to the original values before the averaging.

The reaction orders with respect to C_3H_4 and H_2 for the C_3H_4 hydrogenation in the absence of C_3H_6 were evaluated at 100°C from the reaction rates for four different concentrations in the feed. The reactants were [n% C_3H_4/40% H_2/He balance (n = 0.05, 0.08, 0.13, and 0.2)] and [0.1% C_3H_4/m% H_2/He balance (m = 20, 30, 50, and 80)]. Appropriate amounts of the catalysts and the flow rates were used so that the conversion was appropriate for estimating the reaction orders. Data were obtained 30 min after changing the concentration. Figure S5 shows the double logarithmic plots of the reaction rate versus concentration. The reaction orders were measured twice; their averages are shown in table S1.

Calculation of electronic structures

The electronic structures were calculated using the full-potential linearized augmented plane wave method (*36*). The generalized gradient approximation developed by Perdew *et al.* (*37*) was used for the exchange-correlation potential. The plane wave cutoff was $RK_{max} = 7.0$, where R is the smallest atomic sphere radius and K_{max} is the magnitude of the largest K vector. For the atomic sphere radius, we used 2.22 atomic unit (a.u.) for the 3*d* transition metals and 2.09 a.u. for Ga and Ge. To calculate the electronic structure of each Heusler alloy listed in table S2, we used the model structure with the space group given in the table. The optimized lattice constants are also listed in the table. The lattice vectors for $Co_2Mn_{0.5}Fe_{0.5}Ge$ and $Co_2FeGe_{0.5}Ga_{0.5}$ are $\mathbf{a}' = (\mathbf{a} + \mathbf{b})/2$, $\mathbf{b}' = (-\mathbf{a} + \mathbf{b})/2$, and $\mathbf{c}' = \mathbf{c}$, where $\mathbf{a}$, $\mathbf{b}$, and $\mathbf{c}$ are lattice vectors for the cubic lattice. We used a 20 by 20 by 20 K-mesh for the Brillouin zone integration for ternary alloys such as Co_2FeGe. For quaternary alloys, the K-meshes were chosen so that the size of the K-mesh corresponds to that for the ternary alloys.

The most stable surface of Heusler alloys seems to be a close-packed (110) surface, which has been indicated by calculation for seven types of surfaces, as shown in table S3. To simulate a thin (110) film of Co_2FeGe and Co_2FeGa used for Fig. 5B, we considered a slab in a supercell specified by three primitive vectors: $\mathbf{a}' = (-\mathbf{a} + \mathbf{b})/2 = a(-0.5,0.5,0)$, $\mathbf{b}' = \mathbf{c} = a(0,0,1)$, and $\mathbf{c}' = 7(\mathbf{a} + \mathbf{b}) = a(7,7,0)$, where a denotes the length of the side of the conventional unit cell of a cubic lattice. The film used was constructed on 11 layers with a total thickness of 5$|\mathbf{c}'|$/14 and an empty (vacuum) region with a thickness of 9$|\mathbf{c}'|$/14. We used a = 5.741 and 5.720 Å, which gave a minimum total energy for the bulk ferromagnetic Co_2FeGe and Co_2FeGa, respectively (see table S2). For both films, we estimated the equilibrium positions of the atoms in the direction of $\mathbf{c}'$. The K-mesh adopted was 14 by 10 by 2. See (*38*) for more information.

The d-band center (ε_d) is defined as (*20*)

$$\varepsilon_d = \frac{\int_{-\infty}^{\infty} \varepsilon D(\varepsilon) d\varepsilon}{\int_{-\infty}^{\infty} D(\varepsilon) d\varepsilon} \quad (8)$$

where $D(\varepsilon)$ is the PDOS of the d-band at an energy, ε. We estimated the ε_d values from the sum of $D(\varepsilon)$ for the transition metal components with the integration range from −13.000 to 6.457 eV, which was enough for a relative comparison of ε_d. The ε_d values were estimated from the bulk electronic structures because the calculation of the surface electronic structures for $Co_2Mn_{0.75}Fe_{0.25}Ge$, $Co_2Mn_{0.25}Fe_{0.75}Ge$, $Co_2FeGa_{0.25}Ge_{0.75}$, and $Co_2FeGa_{0.75}Ge_{0.25}$ made it difficult to assume appropriate supercells and slabs and would have very high calculation costs. The difference in DOS between the surface and the bulk originates from symmetry breaking at the surface, which indicates that materials with the same crystal structure and similar component elements make similar changes in the DOS from the bulk to the surface (*39*). Thus, the bulk ε_d values could be used for relative comparisons among our samples.

Hard x-ray photoelectron spectroscopy

HAXPES measurements at room temperature were performed to evaluate the electronic structures experimentally at the BL15XU undulator beamline (*40*) of SPring-8. The sample ingots were cut into about 1-mm by 1-mm by 10-mm rods, fixed on a copper holder using a silver paste, and then placed in a preparation chamber (base pressure, 2.0×10^{-7} Pa) connected with a measurement chamber (base pressure, $<1.0 \times 10^{-7}$ Pa). After evacuation of the preparation chamber, the rods were fractured in situ to obtain a clean surface and then moved into the measurement chamber. The excitation photon energy and total energy resolution were set to 5.95 keV and 240 meV, respectively. The binding energy was referred to the Fermi level of an evaporated gold film. Details of the experimental setup are described elsewhere (*40*). The electric field vector of the incident beam was parallel to the photoelectron trajectory to the analyzer. Because of this geometry, a high-intensity structure originating from the s-bands at binding energies >4 eV is evident in Fig. 4 (B1 and B2) (*22*). We also performed the measurement for $Co_2FeGa_{0.5}Ge_{0.5}$ powders before and after the alkyne hydrogenation in the presence of alkene, which indicated no surface segregation and no carbon deposition (coking or oil production) within the sensitivity, as shown in fig. S7.

SUPPLEMENTARY MATERIALS

Supplementary material for this article is available at http://advances.sciencemag.org/cgi/content/full/4/10/eaat6063/DC1

Supplementary Text

Fig. S1. Results of C_3H_4 hydrogenation in the absence of C_3H_6.

Fig. S2. Details of elemental substitution effects in C_3H_4 hydrogenation in the absence of C_3H_6.

Fig. S3. Results of C_3H_6 hydrogenation.

Fig. S4. An example Arrhenius plot for Co_2FeGa in C_3H_4 hydrogenation in the absence of C_3H_6.

Fig. S5. C_3H_4 reaction rate at 100°C versus feed concentrations in C_3H_4 hydrogenation in the absence of C_3H_6.

Fig. S6. XRD patterns for Heusler alloy samples.

Fig. S7. Core-level HAXPES spectra for $Co_2FeGa_{0.5}Ge_{0.5}$ powders before and after alkyne hydrogenation in the presence of alkene.

Table S1. List of Heusler alloy samples and related information.

Table S2. Information on calculation of electronic structures.

Table S3. List for calculation on surface stability.

REFERENCES AND NOTES

1. F. Heusler, Magnetic-chemical studies *Verh. Dtsch. Phys. Ges.* **5**, 219 (1903).
2. K. Momma, F. Izumi, *VESTA 3* for three-dimensional visualization of crystal, volumetric and morphology data. *J. Appl. Crystallogr.* **44**, 1272–1276 (2011).
3. T. Graf, C. Felser, S. S. P. Parkin, Heusler Compounds: Applications in Spintronics, in *Handbook of Spintronics*, X. Yongbing, D. D. Awschalom, J. Nitta, Eds. (Springer Netherlands, 2016), pp. 335–364.
4. Y. Nishino, H. Kato, M. Kato, U. Mizutani, Effect of off-stoichiometry on the transport properties of the Heusler-type Fe_2VAl compound. *Phys. Rev. B* **63**, 233303 (2001).
5. A. Planes, L. Mañosa, M. Acet, Magnetocaloric effect and its relation to shape-memory properties in ferromagnetic Heusler alloys. *J. Phys. Condens. Matter* **21**, 233201 (2009).
6. M. Yin, J. Hasier, P. Nash, A review of phase equilibria in Heusler alloy systems containing Fe, Co or Ni. *J. Mater. Sci.* **51**, 50–70 (2016).
7. A. P. Tsai, S. Kameoka, Y. Ishii, PdZn = Cu: Can an intermetallic compound replace an element? *J. Phys. Soc. Jpn.* **73**, 3270–3273 (2004).
8. S. Furukawa, T. Komatsu, Intermetallic compounds: Promising inorganic materials for well-structured and electronically modified reaction environments for efficient catalysis. *ACS Catal.* **7**, 735–765 (2017).
9. T. Kojima, S. Kameoka, A.-P. Tsai, Heusler alloys: A group of novel catalysts. *ACS Omega* **2**, 147–153 (2017).

10. A. Borodziński, G. C. Bond, Selective hydrogenation of ethyne in ethene-rich streams on palladium catalysts. Part 1. Effect of changes to the catalyst during reaction. *Catal. Rev.* **48**, 91–144 (2006).
11. A. Borodziński, G. C. Bond, Selective hydrogenation of ethyne in ethene-rich streams on palladium catalysts, part 2: Steady-state kinetics and effects of palladium particle size, carbon monoxide, and promoters. *Catal. Rev.* **50**, 379–469 (200).
12. F. Samimi, Z. K. Modarresi, O. Dehghani, M. R. Rahimpour, A. Bolhasani, Application of response surface methodology for optimization of an industrial methylacetylene and propadiene hydrogenation reactor. *J. Taiwan Inst. Chem. Eng.* **46**, 51–64 (2015).
13. F. Studt, F. Abild-Pedersen, T. Bligaard, R. Z. Sørensen, C. H. Christensen, J. K. Nørskov, Identification of non-precious metal alloy catalysts for selective hydrogenation of acetylene. *Science* **320**, 1320–1322 (2008).
14. M. Armbrüster, K. Kovnir, M. Friedrich, D. Teschner, G. Wowsnick, M. Hahne, P. Gille, L. Szentmiklósi, M. Feuerbacher, M. Heggen, F. Girgsdies, D. Rosenthal, R. Schlögl, Y. Grin, $Al_{13}Fe_4$ as a low-cost alternative for palladium in heterogeneous hydrogenation. *Nat. Mater.* **11**, 690–693 (2012).
15. Y. Liu, X. Liu, Q. Feng, D. He, L. Zhang, C. Lian, R. Shen, G. Zhao, Y. Ji, D. Wang, G. Zhou, Y. Li, Intermetallic Ni_xM_y (M = Ga and Sn) nanocrystals: A non-precious metal catalyst for semi-hydrogenation of alkynes. *Adv. Mater.* **28**, 4747–4754 (2016).
16. T. Kojima, S. Fujieda, G. Kato, S. Kameoka, S. Suzuki, A.-P. Tsai, Hydrogenation of propyne verifying the harmony in surface and bulk compositions for Fe-Ni alloy nanoparticles. *Mater. Trans.* **58**, 776–781 (2017).
17. N. Yoshida, "Catalytic hydrogenation of methylacetylene over group VIII metals: Application of microwave spectroscopy to the analysis of isomeric deuteropropylenes," thesis, Osaka University, Japan (1971).
18. B. Bridier, J. Pérez-Ramírez, Cooperative effects in ternary Cu–Ni–Fe catalysts lead to enhanced alkene selectivity in alkyne hydrogenation. *J. Am. Chem. Soc.* **132**, 4321–4327 (2010).
19. J. K. Nørskov, F. Abild-Pedersen, F. Studt, T. Bligaard, Density functional theory in surface chemistry and catalysis. *Proc. Natl. Acad. Sci. U.S.A.* **108**, 937–943 (2011).
20. A. Vojvodic, J. K. Nørskov, F. Abild-Pedersen, Electronic structure effects in transition metal surface chemistry. *Top. Catal.* **57**, 25–32 (2014).
21. T. Bligaard, J. K. Nørskov, S. Dahl, J. Matthiesen, C. H. Christensen, J. Sehested, The Brønsted–Evans–Polanyi relation and the volcano curve in heterogeneous catalysis. *J. Catal.* **224**, 206–217 (2004).
22. S. Ueda, I. Hamada, Polarization dependent bulk-sensitive valence band photoemission spectroscopy and density functional theory calculations: Part I. 3*d* transition metals. *J. Phys. Soc. Jpn.* **86**, 124706 (2017).
23. L. Brandão, D. Fritsch, A. M. Mendes, L. M. Madeira, Propyne hydrogenation kinetics over surfactant-stabilized palladium nanoclusters. *Ind. Eng. Chem. Res.* **46**, 377–384 (2007).
24. V. Pallassana, M. Neurock, Electronic factors governing ethylene hydrogenation and dehydrogenation activity of pseudomorphic Pd_{ML}/Re(0001), Pd_{ML}/Ru(0001), Pd(111), and Pd_{ML}/Au(111) Surfaces. *J. Catal.* **191**, 301–317 (2000).
25. B. Bridier, N. López, J. Pérez-Ramírez, Molecular understanding of alkyne hydrogenation for the design of selective catalysts. *Dalton Trans.* **39**, 8412–8419 (2010).
26. J. R. Kitchin, J. K. Nørskov, M. A. Barteau, J. G. Chen, Role of strain and ligand effects in the modification of the electronic and chemical properties of bimetallic surfaces. *Phys. Rev. Lett.* **93**, 156801 (2004).
27. E. Roduner, Understanding catalysis. *Chem. Soc. Rev.* **43**, 8226–8239 (2014).
28. G. Sugihara, D.-S. Shigematsu, S. Nagadome, S. Lee, Y. Sasaki, H. Igimi, Thermodynamic study on the langmuir adsorption of various bile salts including taurine and glycine conjugates onto graphite in water. *Langmuir* **16**, 1825–1833 (2000).
29. E. Garrone, B. Bonelli, C. O. Areán, Enthalpy–entropy correlation for hydrogen adsorption on zeolites. *Chem. Phys. Lett.* **456**, 68–70 (2008).
30. A. Hellman, K. Honkala, Including lateral interactions into microkinetic models of catalytic reactions. *J. Chem. Phys.* **127**, 194704 (2007).
31. A. M. Efstathiou, C. O. Bennett, Enthalpy and Entropy of H_2 Adsorption on Rh/Al_2O_3 Measured by Temperature-Programmed Desorption. *J. Catal.* **124**, 116–126 (1990).
32. M. Krajčí, J. Hafner, Complex intermetallic compounds as selective hydrogenation catalysts – A case study for the (100) surface of $Al_{13}Co_4$. *J. Catal.* **278**, 200–207 (2011).
33. M. Krajčí, J. Hafner, Intermetallic compounds as selective heterogeneous catalysts: Insights from DFT. *ChemCatChem* **8**, 34–48 (2016).
34. M. Krajčí, A.-P. Tsai, J. Hafner, Understanding the selectivity of methanol steam reforming on the (111) surfaces of NiZn, PdZn and PtZn: Insights from DFT. *J. Catal.* **330**, 6–18 (2015).
35. V. R. Stamenkovic, B. S. Mun, M. Arenz, K. J. J. Mayrhofer, C. A. Lucas, G. Wang, P. N. Ross, N. M. Markovic, Trends in electrocatalysis on extended and nanoscale Pt-bimetallic alloy surfaces. *Nat. Mater.* **6**, 241–247 (2007).
36. A. P. Blaha, K. Schwarz, G. K. H. Madsen, D. Kvasnicka, J. Luitz, *WIEN2k, An Augmented Plane Wave + Local Orbitals Program for Calculating Crystal Properties* (Karlheinz Schwartz, Techn. Universität Wien, Austria, 2001).
37. J. P. Predew, K. Burke, M. Emzerhof, Generalized gradient approximation made simple. *Phys. Rev. Lett.* **77**, 3865–3868 (1996).
38. S. Fujii, Electronic and magnetic properties of (110) films of half-metallic heusler Fe_2CrSi. *IEEE Trans. Magn.* **50**, 1001003 (2014).
39. A. P. Tsai, S. Kameoka, K. Nozawa, M. Shimoda, Y. Ishii, Intermetallic: A pseudoelement for catalysis. *Acc. Chem. Res.* **50**, 2879–2885 (2017).
40. S. Ueda, Application of hard X-ray photoelectron spectroscopy to electronic structure measurements for various functional materials. *J. Electron Spectros. Relat. Phenomena* **190**, 235–241 (2013).

Acknowledgments: We are grateful to K. Nozawa of Kagoshima University for helpful discussion regarding the relation between the electronic structure and catalysis and to H. Iwamoto and R. Tsukuda of Tohoku University for help in the HAXPES measurement performed at BL15XU at SPring-8 under the approval of NIMS Synchrotron X-ray Station (proposal no. 2017B4905). **Funding:** A part of this work was supported by the Hattori Hokokai Foundation, the Iwatani Naoji Foundation, the Noguchi Institute, and NIMS microstructural characterization platform as a program of "Nanotechnology Platform" (project no. 12024046) of the Ministry of Education, Culture, Sports, Science and Technology (MEXT), Japan. We also thank the support from Dynamic Alliance for Open Innovation Bridging Human, Environment and Materials and the Frontier Research Institute for Interdisciplinary Sciences of Tohoku University. **Author contributions:** T.K. designed this research, performed all experiments and their analyses, and wrote the manuscript. S.K. and A.-P.T. supported and discussed the experiments and the analyses. S.F. performed the calculation of electronic structure and wrote the method of calculation in the manuscript. S.U. performed the HAXPES measurement and its analysis together with T.K. All authors discussed the results and supported the manuscript writing. **Competing interests:** T.K., S.K., and A.-P.T. are authors on a patent application related to this work filed by Tohoku University (JP patent application no. 2017–220616, filed on 16 November 2017). All other authors declare that they have no competing interests. **Data and materials availability:** All data needed to evaluate the conclusions in the paper are present in the paper and/or the Supplementary Materials. Additional data related to this paper may be requested from the authors.

Submitted 16 March 2018
Accepted 10 September 2018
Published 19 October 2018
10.1126/sciadv.aat6063

Citation: T. Kojima, S. Kameoka, S. Fujii, S. Ueda, A.-P. Tsai, Catalysis-tunable Heusler alloys in selective hydrogenation of alkynes: A new potential for old materials. *Sci. Adv.* **4**, eaat6063 (2018).

ScienceAdvances

Catalysis-tunable Heusler alloys in selective hydrogenation of alkynes: A new potential for old materials

Takayuki Kojima, Satoshi Kameoka, Shinpei Fujii, Shigenori Ueda and An-Pang Tsai

Sci Adv **4** (10), eaat6063.
DOI: 10.1126/sciadv.aat6063